Scatter Correction in Cone-Beam Breast Computed Tomography: Simulations and Experiments

G. Mettivier, N. Lanconelli, S. Lo Meo, and P. Russo, *Member, IEEE*

***Abstract*—In Cone-Beam Computed Tomography (CBCT) the X-ray scatter control and reduction is one of the major challenges because CBCT is less immune to scatter than fan-beam CT. In breast volume imaging, studies on Cone-Beam Breast Computed Tomography (CBBCT) have shown the necessity to implement an efficient scatter reduction technique for a successful implementation of a breast CT scan using cone-beam geometry. X-ray scatter reduces image contrast, increases image noise and introduces reconstruction artifacts. A method for scatter evaluation through Monte Carlo simulations is investigated, leading to a scatter correction procedure applied to measured projections via subtraction of the simulated scatter component. Simulations are compared with measurements performed with a CBBCT prototype scanner. This paper presents the evaluation of the method through phantom studies on a cylindrical and on a hemi-ellipsoidal PMMA test object of 120- or 140-mm diameter at its base, simulating the pendant breast. The results indicate that this correction method is effective to reduce and correct X-ray scatter, with no increase of noise in the CT images. The cupping artifact due to scatter was reduced by a factor 3 (from 23% to 7%) for the hemi-ellipsoidal phantom of 140-mm diameter. Correspondingly, the relative noise in the CT slices remains constant to about 3%; the figure of merit for evaluating the correction efficacy was 98% of the ideal case. We discuss the application of this procedure to model breasts characterized in terms of few parameters, as indicated by recent published results of breast anatomy characterization derived from CBBCT patient data, from which a possible parametric breast size model in terms of bra cup size can be set forth. The scatter correction could be applied to projections from patient scans obtained with a breast holder, on the basis of a pre-determined database of simulated scatter distributions corresponding to the breast holder size, shape and estimated volume glandular fraction, for given beam quality and scanner geometry.**

***Index Terms*—Computed tomography, Monte Carlo methods, X-ray scattering.**

I. Introduction

CONE-BEAM computed tomography (CBCT) has been introduced almost three decades ago, but only in recent years there has been a trend for true "volumetric" imaging, where the width of the collimated x-ray beam is extended to the entire Field-of-View (FOV) of interest. The development of flat-panel detectors and other imaging devices has given rise to numerous cone-beam CT systems for many different applications [1]–[6].

Among these applications, the development of research/clinical CBCT scanners dedicated to female breast X-ray imaging (Cone-Beam Breast Computed Tomography, CBBCT) has been explored as a potential strategy for breast cancer screening and diagnosis [7]–[12], [50], [13]. This emerging imaging technology might provide a better visualization and diagnosis of early stage breast cancer thanks to fully 3D visualization of breast anatomy. Clinical trials [14]–[16] ongoing at two large University medical centers (University of California, Davis and University of Rochester) have shown the great potential of this experimental imaging technique, despite nontrivial technological aspects in the realization of high performance dedicated scanners and in the artifact-free cone-beam CT reconstruction process.

In CBCT the x-ray scatter control and reduction is one of the major challenges because this technique is less immune to scatter than fan-beam CT. X-ray scatter reduces image contrast, increases image noise and introduces reconstruction artifacts such as inaccuracy of CT numbers and cupping in the reconstructed CT slices.

Strategies for scatter reduction in CBCT include pre-processing methods, which use only the projections and attempt to prevent scatter from reaching the detector, such as antiscatter grids or air gaps; post-processing methods, with supplementary measurements based on an estimation of the scatter contribution, such as Beam Stop Arrays (BSA); scatter simulation methods, usually using Monte Carlo (MC) methods.

Literature on scatter estimation and correction in CBCT is vast and has recently been reviewed [17], [18]. Scatter magnitude is an increasing function of the transverse and longitudinal FOV (i.e., dependent on fan angle and cone angle, respectively) and a function of beam quality and tissue composition, so that there are some differences in the task of scatter correction between CBCT and CBBCT. In CBCT imaging, phantoms of size 160 mm ("head") or 320 mm ("body") are typically used and values of scatter-to-primary ratio (SPR) in excess of 100% are reported (at 120 kVp) [19]. When imaging the breast (typical diameters at chest wall between 110 and 140 mm), comparatively less tissue volumes are irradiated and lower SPR values are reported (e.g., axial $\mathrm{SPR} \cong 0.5$ at 80 kVp for a breast of 140 mm diameter and 50% glandular fraction [20]). Streak artifacts (from high density structures like bones) are usually not present in the breast volume, apart from calcifications of millimeter or sub-millimeter size. In CBBCT less penetrating X-ray beams

Manuscript received July 20, 2011; revised October 07, 2011, December 23, 2011, and April 05, 2012; accepted May 23, 2012. Date of publication July 10, 2012; date of current version October 09, 2012.

G. Mettivier and P. Russo are with the Università di Napoli Federico II, Dipartimento di Scienze Fisiche, and INFN, Sezione di Napoli, I-80126 Napoli, Italy (e-mail: mettivier@na.infn.it).

N. Lanconelli and S. L. Leo are with the Alma Mater Studiorum-Università di Bologna, Dipartimento di Fisica and INFN, Sezione di Bologna, I-40127 Bologna, Italy.

Color versions of one or more of the figures in this paper are available online at http://ieeexplore.ieee.org.

Digital Object Identifier 10.1109/TNS.2012.2201955

0018-9499/$31.00 © 2012 IEEE

(e.g., 50–80 kVp) are typically used than in CBCT (e.g., 80–120 kVp), so that also multiple scatter is less important; moreover, beam hardening is less of concern in CBBCT, due to the comparative lower spectral extent of the poly-energetic X-ray beam. On the other hand, under-table CBBCT scanners are compact ($\cong$ 800 mm scanner diameter) and air gaps could be significantly shorter than in CBCT scanners ($\cong$ 1600 mm scanner diameter).

Various authors investigated scatter amount and effects for the dedicated CBBCT scanners [20]–[22]. In these studies the SPR metric was investigated as a function of a number of clinically relevant parameters for breast CT imaging, including X-ray beam energy, cone angle, breast diameter, breast composition, isocenter-to-detector distance, and antiscatter grid ratio. Results indicated that the SPR levels for the average breast size (140-mm diameter) are quite high ($\sim$0.5–0.6) and increase as the diameter of the phantom increases (SPR $\sim$1, breast diameter $=$ 180 mm) [20]. The X-ray beam energy and the phantom composition have only minimal impact on the measured SPR [20]. These high SPR values reported suggest that efficient scatter rejection and/or correction techniques are required for the successful implementation of breast CT using cone-beam geometry. The use of antiscatter grids in CBBCT was investigated by Kwan *et al.* [20]. The dose penalty due to the use of a grid (primary transmission factor $>$56% for grid ratios $>8:1$) suggested that conventional grid technology may be inappropriate with respect to the need for low dose breast imaging, particularly for screening exams. Moreover, in agreement with the results reported in [23], those authors suggest that use of antiscatter grids is detrimental in a high resolution CBBCT imaging [20].

Kwan *et al.* [20] studied, moreover, the use of an air gap and reported a maximum reduction of the SPR from $\cong$ 1.0 to $\cong$ 0.8 with an air gap increase of 100 mm, at 80 kVp and for large breast sizes (breast diameter $=$ 180 mm) with concern about the practical issue of maintaining a balance between scatter reduction, photon fluence, and the compact dimensions of the scanner.

An example of the pre-processing strategy is the correction method proposed in [24]. This method is based on direct scatter estimation in each projection from pixel values near the edge of the detector behind collimator leaves. This technique enables an accurate estimation of the mean scatter level, but does not take into account the object heterogeneities in the FOV. However, in CBBCT with under-table irradiation geometry, the application of this algorithm is not possible for evaluating the scatter in the longitudinal direction (i.e., from chest wall to nipple) because the presence of collimator shadows on the side of the chest wall would impede the imaging of this critical region in breast exams.

Cai *et al.* [25] suggested an algorithm based on scatter estimation using a reduced set of supplementary projections acquired with a BSA by exploiting the breast geometrical symmetry. In the beam-stop method an array of radio-opaque absorbers is placed in the beam to absorb primary radiation. Scattered radiation images are then calculated by interpolation and subtracted from acquisitions. However this technique requires additional tomographic acquisition and therefore leads to an increase in the x-ray dose and acquisition time.

Several digital methods based on the MC simulation of the scattering distribution have been proposed for scatter investigation in CBCT [26]–[28], as introduced e.g., by Boone and Seibert for diagnostic radiology [29]. Simulation-based scatter correction strategies require no extra dose to the patient or supplementary measurements, yet providing efficient scatter removal. Their strongest limitation is the high computational demand due to the need of launching a large number of photon histories for a realistic simulation, requiring, e.g., almost three weeks of CPU time [30]. Various techniques have been applied to reduce the calculation time, e.g., down to just a few minutes [31]–[36].

In this work we performed MC simulations of CT scans of PolyMethylMethaAcrylate (PMMA) phantoms (the detector response is not simulated), validate them through measurements and apply a scatter correction procedure based on the subtraction of simulated scatter components from measured projection images. This work extends our previous investigation on scatter evaluation with MC simulation on PMMA phantoms, by applying a scatter correction procedure after the scatter evaluation. We show the algorithm's efficiency using experimental cone-beam acquisitions obtained using our CBBCT prototype for two different shaped phantoms. We also discuss the clinical application of this technique to scans obtained with the patient breast laid down in a breast holder and corresponding use of simulated scatter projections pre-determined on the basis of the given breast shape, size and volume glandular fraction.

II. Material and Methods

A. Prototype System

The CBBCT unit used for the experiment was a prototype bench-top scanner assembled at Federico II University (Napoli, Italy) for evaluation and for laboratory tests of various optimization techniques for CBBCT (Fig. 1(a)). The prototype is described in detail elsewhere [12], [50], [13] and is characterized by the computer-control of all its elements: *i*) the X-ray tube (W anode, operated at 80 kVp, 0.25 mA, continuous output, 1.8 mm Al intrinsic filtration and 0.2 mm Cu added filtration, measured Half Value Layer (HVL) 5.6 mm Al); *ii*) the CsI:Tl CMOS flat panel detector (FPD) (Hamamatsu C7942CA-02, 12×12 cm^2 area, 50 μm pixel pitch, 0.15-mm thick scintillator layer, frame rate up to 2 fps at 1×1 pixel binning and up to 9 fps at 4×4 binning); *iii*) the step-motor translation and rotation stages with eight degrees of freedom. CT scans were done in step-and-shoot mode. Commercial cone-beam back-projection software was available implementing the Feldkamp-Davis-Kress (FDK) algorithm [37] (COBRA, Exxim Computing Corporation, Pleasanton, CA, USA). The scanner works in step-and-shoot as well as in continuous acquisition mode.

B. Simulation

The GEANT4 code system (ver. 4.9.0, with the standard transport model and library of electromagnetic interactions, EMStandard library) was used to model the CBBCT scans obtained with the apparatus described in Section II.A. The Standard EM package provides simulation of ionization,

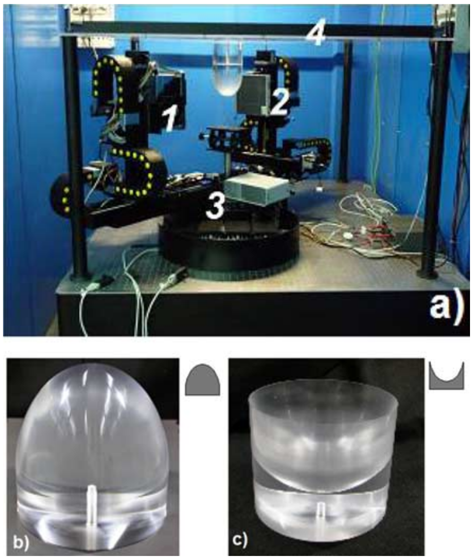

Fig. 1. (a) Photo of the first version of the CBBCT bench-top prototype at Federico II University in Napoli, used in this work, showing the rotating gantry (3), the X-ray tube (1), the flat panel detector (2) and PMMA breast phantom hanging from the PMMA bed (4). The scanner is mounted on an optical bench (1.5×1.8 m^2) and housed in a shielded (3 mm Pb) cabinet. The scanner has fully computer-controlled X-ray tube, mechanical positioning systems with eight degrees of freedom, and flat panel X-ray digital detector. (b) Photo of hemi-ellipsoidal PMMA breast phantom of 140-mm diameter. (c) Photo of a prototype breast holder in the form of a hollow PMMA cup with hemi-ellipsoidal shape, with a cylindrical base.

bremsstrahlung and other Electro-Magnetic interactions of particles with matter. More details about the physics implemented in the EM Standard library and its application can be found in [38]–[40].

Simulations and acquisitions were performed in half cone-beam irradiation geometry (Fig. 2) at an X-ray beam voltage of 80 kVp at the same exposure level of 7 μGy air kerma per view at the isocenter. A number of 360 views were simulated, equally spaced over 360 deg in a circular orbit around the phantoms, for a total of $7\ \mu\text{Gy} \times 360 = 2.5$ mGy air kerma at the scanner isocenter.

For the W anode X-ray tube, the spectrum calculated by Boone's TASMIP code [41] was used for the 80 kVp beam with 1% ripple, to which 1.8 mm Al and 0.2 mm Cu filtrations were added. The average beam energy was 48.5 keV (Fig. 3).

The photons impinging on the detector were recorded and separated as primary photons (defined as those that did not undergo any scattering within the phantom) and scattered photons (defined as those encountering at least one Compton or Rayleigh scattering event in the phantom). We determined image distributions of the energy fluence incident on the detector (MeV/mm^2) by scoring the total energy (MeV) of the primary and of the scatter components at the entrance of the detector in 1×1 mm^2 equivalent pixels over a projection area of 240×240 mm^2. The values of energy fluence per pixel are proportional to the simulated total air kerma at isocenter (2.5 mGy) and could be scaled appropriately to any given exposure level. Since we did not model the production and collection of scintillation light in the FPD, a scaling factor was applied to the simulated image in order to compare the simulated and measured images. The total

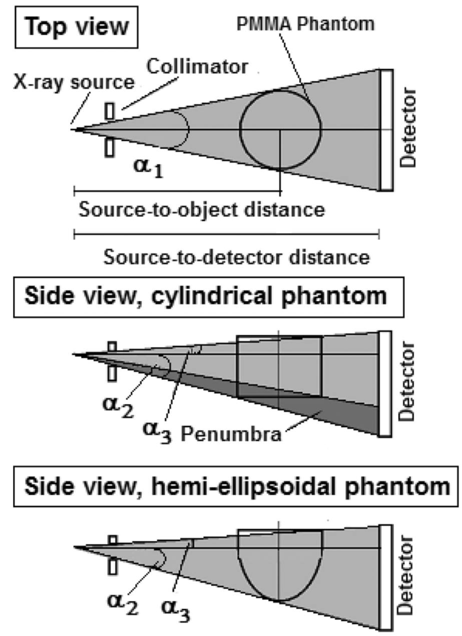

Fig. 2. Top and lateral view of the half cone-beam geometry, where α_1 and $\alpha_2 + \alpha_3$ are the fan angle and cone angle, respectively. Cylindrical and hemi-ellipsoidal PMMA phantoms, of 120- or 140-mm diameter at their base, have been imaged. The effect of the presence of a "penumbra" by cone beam irradiation of the cylindrical phantoms is illustrated (the angles indicated are the minimum required for phantom coverage at the isocenter).

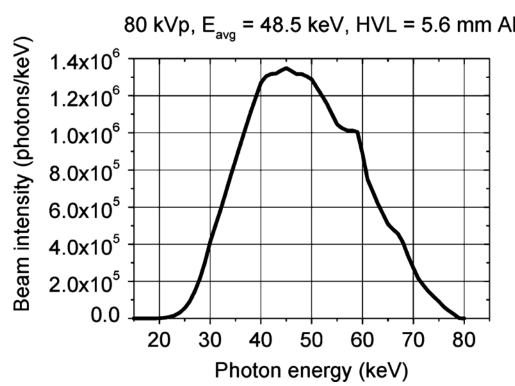

Fig. 3. Simulated spectrum of the X-ray source.

(i.e., primary+scatter), primary and scatter images can thus be obtained from the simulations. This approach assumes independence of the FPD response on slight variations of the shape of the beam produced by beam hardening, upon transmission through the samples.

C. Measurements

CT scans of a homogeneous PMMA cylinder and of a PMMA hemi-ellipsoidal phantom were performed with the prototype described in Section II.A. Experimental results of this set-up (which simulates the scan of an uncompressed pendant breast) were compared with MC simulations. Measurements were performed with the half cone-beam irradiation geometry, at a tube voltage of 80 kVp and with a tube current of 0.25 mA. Phantoms were placed at the scanner isocenter at a source-to-detector distance (SID) of 505 mm and a source-to-object distance of

TABLE I
IMAGING GEOMETRY AND ACQUISITION/RECONSTRUCTION PARAMETERS

Scanner geometry	
Source to isocenter distance	385 mm
Source to detector distance	505 mm
Isocenter to detector distance	120 mm
Magnification factor	1.31
Total beam fan angle α_1, 240×240 mm^2 FOV	25.4 deg
Total beam cone angle α_2+α_3, 240×240 mm^2 FOV	25.4 deg
CT Simulation	
Tube voltage	80 kVp
Air Kerma per view (isocenter)	7 μGy
Total Air Kerma (isocenter)	2.5 mGy
Total beam fan angle α_1, 240×240 mm^2 FOV	25.4 deg
Total beam cone angle α_2+α_3, 240×240 mm^2 FOV	25.4 deg
No. of projections simulated over 360 deg	360
Vertical position of focal spot	at chest wall
CT acquisition	
Tube voltage	80 kVp
Tube current	0.25 mA
Exposure time 120×120 mm^2 field	60 s
Total exposure time	4×60 s
Total tube load	15 mAs
Air kerma per view (isocenter)	7 μGy
Total Air Kerma (isocenter)	2.5 mGy
No. of projections over 360 deg	360
Detector pixel size, 4×4 binning	0.2×0.2 mm^2
Vertical position of focal spot	at chest wall
Image processing and reconstruction	
Detector bad pixel removal for projections	2×2 median filter
Cone-beam filtered back-projection algorithm	FDK
Reconstruction filter	Ramp
Reconstruction volume	160×160×160 mm^3
Voxel size	0.5×0.5×0.5 mm^3
Gaussian smoothing filter	2 pixel σ

385 mm. Hence, the air gap between phantom diameter and detector is only 50 mm for the 140-mm diameter. System magnification was 1.31 at the isocenter. The short SID was chosen in combination with a low magnification in order to limit the field coverage for the detector. To acquire projections with the same FOV (240×240 mm^2) as in simulated projections, with the limited area (120×120 mm^2) X-ray detector, successive horizontal and vertical translations of the detector were made in the image plane, in a 2×2 mosaic. The scan time for a detector frame was 60 s (tube load, 15 mAs) and 240 s for a 240×240 mm^2 scan (Table I). The air kerma was measured at isocenter without the phantom, as 2.5 mGy per scan.

D. Breast Phantoms

The influence of the proposed scatter correction algorithm on image quality was assessed using a simple cylindrical PMMA phantom for examination of cupping artifacts and noise. First, we also simulated a PMMA cylinder with a diameter of 140 mm and 100 mm height ($\mathrm{volume} = 1.539 \times 10^3$ mm^3); an identical phantom was manufactured from a rod of PMMA for measurements with the CT set-up. In CBBCT, the breast is imaged in a pendant position without compression. Hence, for a more realistic breast phantom we simulated a PMMA phantom shaped as a hemi-ellipsoid of semi-axes 70 mm and 95 mm on a cylindrical base of 140 mm diameter and 35 mm height ($\mathrm{volume} = 1.513 \times 10^3$ mm^3). Two PMMA phantoms with identical shape and size were manufactured (Fig. 1(b)); the first one was completely homogeneous and made from one block while the second one was made of two halves held together. In one-half we realized, at mid-plane, six air-filled cylindrical cavities ($\mathrm{diameter} = 12$ mm, $\mathrm{depth} = 1$ mm) and two sets of resolution details in the form of cylindrical holes with axis perpendicular to system rotation axis, with bore size of 1, 1.5 and 2 mm. These air-filled holes were used as high contrast details (air in PMMA).

A last phantom used in the simulations was a hemi-ellipsoid (semi-axes 70 mm and 90 mm on a cylindrical base of 140-mm diameter and 35-mm height) made of breast tissue ($\mathrm{density} = 0.959$ g/cm^3) with a 13.2% glandular fraction and 86.8% adipose fraction according to ICRU 44 definitions of glandular tissue ($\mathrm{density} = 1.02$ g/cm^3) and adipose breast tissue ($\mathrm{density} = 0.95$ g/cm^3) [42].

E. Image Reconstruction

The CBBCT acquisitions consisted of 360 projections taken at 1 deg intervals in a circular orbit around the phantom, placed at the scanner isocenter. The acquired projection image is first dark corrected by subtracting the dark image offset, and then gain-corrected by dividing it pixel by pixel by a uniformly exposed field. This image is then multiplied by the arbitrary factor 1000.

The raw projection data were acquired at 560×586 pixels (4×4 pixel binning of 0.05-mm pitch detector pixels at 14 bit/pixel) and then a smoothed with a Gaussian kernel of 2 pixel sigma. In order to compare measurements with simulations, the projections were off-line further binned 5×5 to obtain the dimensions (1×1 mm^2) of simulated pixel.

Volumes of $160 \times 160 \times 160$ mm^3 ($0.5 \times 0.5 \times 0.5$ mm^3 voxels) were reconstructed with the cone-beam FDK filtered back-projection algorithm (ramp filter). A summary of the acquisition and reconstruction parameters is given in Table I. No beam hardening or cupping artifact correction was applied at this stage.

All images were processed with the ImageJ public-domain software (http://rsbweb.nih.gov/ij/).

F. Figure of Merit

Following [19], we quantify the image uniformity by a simple metric, t_{cup}, defined in relation to the magnitude of the cupping artifact:

$$t_{\mathrm{cup}} \equiv \frac{(\mu_p - \mu_c)}{\mu_p} \times 100$$

where μ_{p} and μ_{c} refer to the mean over a Region of Interest (ROI) (of 20×20 voxels, about 100×0.5 mm^3) of the reconstructed attenuation coefficient, μ, calculated near the edge (μ_{p}) or near the center (μ_{c}) of the phantom in an axial image, respectively. Image Noise was defined as:

$$\mathrm{Noise} \equiv \frac{\sigma_C}{\mu_C} \times 100$$

where σ_c is the standard deviation of the attenuation coefficient values in an ROI at the centre of the CT slice image. The contrast ΔHU in the CT image

$$\Delta\text{HU} \equiv |\mu_D - \mu_B|$$

(in Hounsfield units, HU) was calculated as the absolute difference between the mean CT number values measured in an ROI of the same diameter in the detail (μ_D) and in the background (μ_B). The Contrast to Noise Ratio (CNR), as:

$$\text{CNR} \equiv \frac{|\mu_D - \mu_B|}{\sigma_B}$$

where σ_B and μ_B are, respectively, the standard deviation and the mean value of the CT number values in an ROI in the background and μ_D is the mean value in an ROI of the same diameter in the detail.

Following [43], we define the figure of merit, Q, for evaluating the efficacy of the proposed scatter correction:

$$Q \equiv \frac{(\text{RMSD}_\text{measured} - \text{RMSD}_\text{corrected})}{\text{RMSD}_\text{measured}},$$

where the Root Mean Square Difference (RMSD) is:

$$\text{RMSD} \equiv \sqrt{\frac{1}{n}\sum_{i=1}^{n}(\text{CT}\#_i - \text{CT}\#_\text{ideal})^2}.$$

In this formula, n is the number of the considered voxels in the selected ROI, $\text{CT}\#_i$ is the CT number in the i-th voxel of the ROI and $\text{CT}\#_\text{ideal}$ is the CT number of PMMA at 80 kVp, evaluated on the reconstructed slices obtained from the simulated primary component. With this figure of merit, $Q = 0$ corresponds to the uncorrected volume and $Q = 1$ to the ideal reconstructed volume.

G. Scatter Correction Method

The method for scatter correction is based on the off-line creation of a dataset of scatter projection images. The algorithm is described in Fig. 4 and is composed of six steps. First, a set of CBBCT projections $I(i,j)$ is measured. The second step consists of the retrieval from the scatter database of the correspondent simulated scatter projection $S(i,j)$. The scatter projections $S(i,j)$ are then subtracted from the original measured projections, to obtain scatter corrected projections $C(i,j)$. These are then reconstructed to obtain the scatter-corrected reconstruction $R(x,y)$ in the tomographic planes.

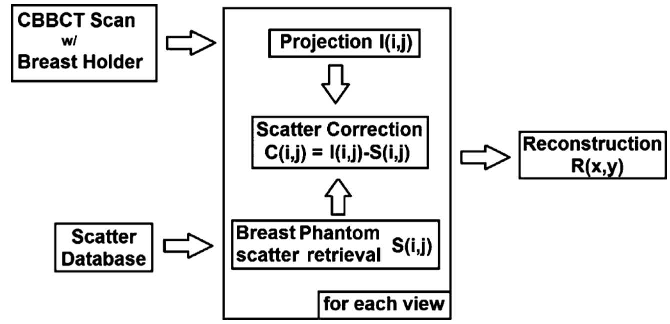

Fig. 4. Algorithm's flow chart. Measured projections are corrected by subtraction of a simulated scatter component extracted from a database of predetermined scatter images for a breast phantom for the given breast size, composition and shape and for given scan geometry. Then, conventional cone-beam reconstruction is performed on the dataset of corrected projections. To assure geometrical correspondence between actual breast and simulated phantoms a breast holder of suitable size is used during the CT scan.

III. Results

A. Simulation

Before evaluating the scatter correction procedure, it is useful to analyze the spatial distribution of the simulated and measured projections, in order to evaluate the quality and quantity of scatter and appreciate the proposed correction. Fig. 5 shows projection images of the simulated primary, scatter, total distributions and of SPR, together with measured and of scatter-corrected projections, at 80 kVp, for a PMMA cylinder of 140-mm diameter (upper row), and for a PMMA hemi-ellipsoid of 140-mm diameter (bottom row). For scatter correction, the simulated "scatter" images were subtracted from the corresponding measured projections, after being scaled by a suitable factor which takes into account the FPD detection. The corresponding horizontal profiles along a diameter are shown in Fig. 6, in which a comparison is provided for all the profiles in the case of the ϕ140 mm cylindrical phantom.

This figure shows a good agreement between MC simulation data ($P+S$ components) and real acquisition (measured projections, M), as indicated by the closeness of the profiles $P+S$ and M: the relative deviation $(P+\text{S}-M)/(P+S)$ is $-(2\pm 2)\%$ $(\text{mean} \pm \text{standard deviation})$ in the 120-mm wide central portion of the profile. This is taken as an indication of the validity of the simulation code. In the same central zone of the profiles in Fig. 6, we calculated the relative difference $((P-C)/P)$ in percent between the corrected (C) profile and the profile of the simulated primary distribution for the cylindrical phantom (P): this difference is $-(0.6\pm 4)\%$ in the profile evaluated. The vertical and horizontal profiles for 140-mm diameter phantoms (cylinder and hemi-ellipsoid) are reported in Fig. 7. The vertical profiles were determined along the vertical central axis of the phantom (i.e., from the "chest wall" to the "nipple") as line profiles averaged over 20 adjacent image columns. The horizontal profiles were measured at 100 mm from the top base as the line profile averaged over 20 image rows. In Fig. 7, the dotted vertical lines indicate the vertical and horizontal phantom dimensions, including magnification.

B. Scatter Correction

The corrected projection images have been back-projected with the FDK algorithm. Fig. 8 shows the CT map of a central slice in the 140-mm cylindrical phantom, reconstructed using either the simulated primary and total components (Figs. 8(a), (b) and corresponding line profiles in Fig. 9), or the measured projections (Fig. 8(c)).

While CT slices reconstructed using only the primary component exhibit almost no cupping (see line profile marked as

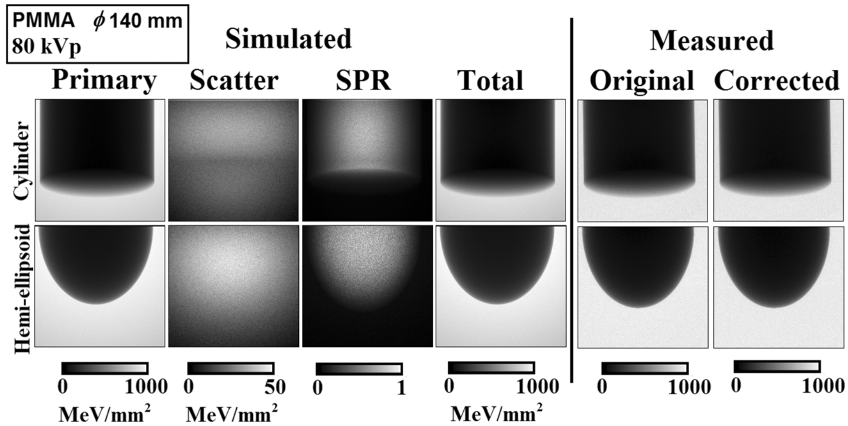

Fig. 5. Simulated projection images (distribution of primary, scatter, primary+scatter and SPR) and measured projection images (original raw data and corrected data), at 80 kVp, of the ϕ140 mm PMMA cylindrical phantom (upper row) and of the PMMA half-ellipsoidal phantom (lower row, ϕ140 mm at the base). The number of photon histories in the simulation was determined so as to correspond to a total air kerma of 2.5 mGy at the scanner isocenter, where the axis of the phantom was positioned. The total energy fluence reaching the detector (in MeV/mm^2) was scored in the simulation.

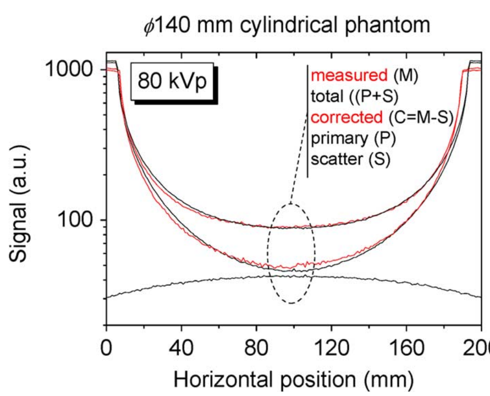

Fig. 6. Profiles along the horizontal direction (at a distance of 50 mm from the top base) of the simulated, measured and scatter-corrected projections at 80 kVp of 140-mm diameter PMMA cylindrical phantom.

"P" in Fig. 9), the reconstruction with the simulated total beam shows a significant cupping artifact (profile "$P{+}S$" in Fig. 9); a similar cupping is shown in this figure for the measured data (profile "M").

The $t_{\rm cup}$ and Noise parameters relative to the 140-mm diameter cylindrical phantom were evaluated on the CT slices in Fig. 8, where $t_{\rm cup} = 25\%$ and $\text{Noise} = 3\%$ (Table II) for the uncorrected CT data (Fig. 8(c)). After application of the scatter correction procedure, we obtained the CT slice shown in Fig. 8(d) and the corresponding line profile ("C") in Fig. 9. This slice and the corresponding profile show a reduced cupping ($t_{\rm cup}$ reduced from 25% before correction, to 6%), as a result of the scatter removal procedure (Table II), and the same noise value (3%). The figure of merit Q, evaluated on a centered circular ROI of 140-mm diameter in the slices in Fig. 8, is $Q = 0.98$ (Table II).

A similar analysis was done on the CT slices simulated and measured for the hemi-ellipsoidal phantom (ϕ140 mm). Horizontal line profiles for the measured and scatter-corrected slices (selected at a height in the phantom where its axial diameter is 118 mm) are shown in Fig. 10. As evident in this figure, and shown in Table II, $t_{\rm cup}$ and Noise figures show a significant variation: an improvement from 23% to 7% in terms of uniformity, and from 3% to 2% in terms of noise. The calculated value for estimating the efficacy of the correction was $Q = 0.96$.

A scan of the hemi-ellipsoidal phantom (ϕ140 mm) containing contrast details was performed, with reconstruction performed either directly or with scatter correction of the projections; coronal and axial slices are shown in Fig. 11. The corresponding average line profiles along the phantom diameter across the details are shown in Fig. 12(a).

The contrast evaluated on the 2-mm size air-filled detail was $\Delta\text{HU} = 455$ in the measured slice and $\Delta\text{HU} = 898$ after correction: this is attributed to the scatter removal procedure which increases the detail contrast through correction of the cupping artifact (Fig. 12(a)). Improvement in image contrast for these high-contrast details can be observed for 2.0 mm as well as for 1.5 and 1.0 mm details, though to a lower extent (Fig. 12(b)): for the 1-mm holes, the contrast ΔHU increased from 245 to 346 HU (a 41% increment). It could be expected that some contrast improvement after scatter compensation could similarly be present also for microcalcifications (size lower than 0.5 mm), in an actual breast scan. The CNR was also evaluated for this detail: $\text{CNR} = 17$ for measured scan and 15 for corrected scan; thus indicating that the contrast improvement coupled to the observed increase of noise keeps almost constant the CNR. As regards the effect of the scatter correction on the CT spatial resolution, Fig. 12(b) shows by simple visual inspection that the size of the details in the reconstructed slices is practically unaffected by the correction procedure.

C. *Breast Tissue vs. PMMA*

In order to compare the simulation and the measurements with a more realistic condition in which the phantom material is a model breast tissue, a simulation has been done for a breast phantom with a hemi-ellipsoidal shape of 140-mm diameter and 13% glandularity, with the remaining adipose fraction of 87%. Indeed, recent biometrical data [44] indicate an average Volume Glandular Fraction (VGF) of about 13% for medium to large-sized breasts, as resulted from the analysis of CBBCT scans in patients. Simulated projections for a 140-mm diameter hemi-ellipsoidal phantom made of PMMA or of 13–87

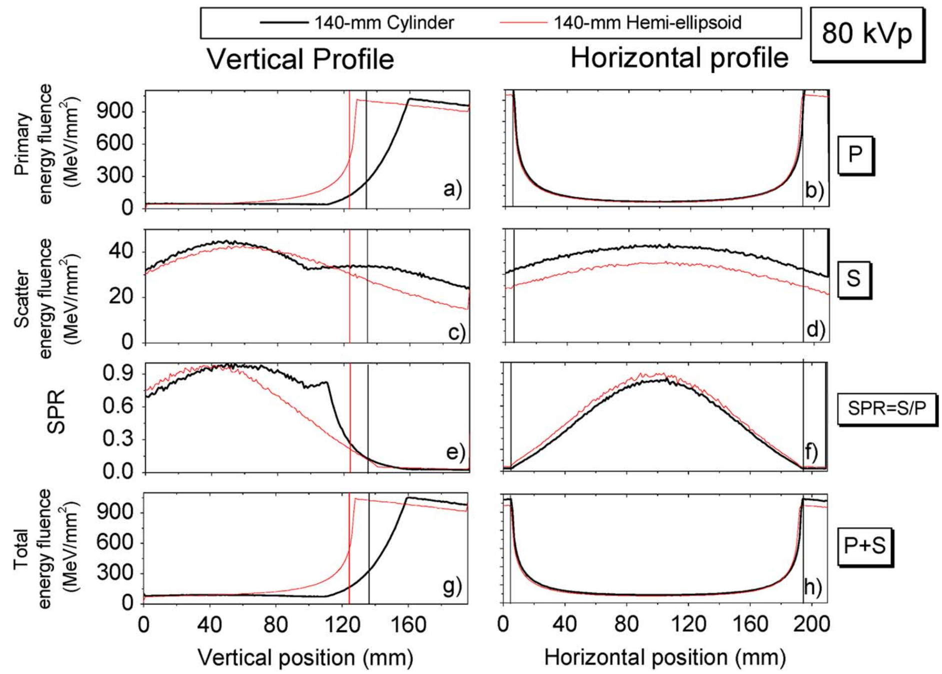

Fig. 7. Vertical (a), (c), (e), (g) and horizontal profiles (b), (d), (f), (h) along the primary (P), scatter (S), total $(\mathrm{P} + \mathrm{S})$ and SPR simulated images reported in Fig. 5 for the cylindrical phantom (black line) and for the hemi-ellipsoidal phantom (red or lighter line) of 140-mm diameter, at 80 kVp. The vertical profiles were determined along the vertical central axis (from the "chest wall" to the "nipple") as the average profiles of 20 image columns. The horizontal profiles (along the detector FOV) were measured at 100 mm from the top base as the average profile of 20 image rows. The solid vertical lines indicate the vertical and horizontal phantom dimensions, including magnification $(M = 1.31)$.

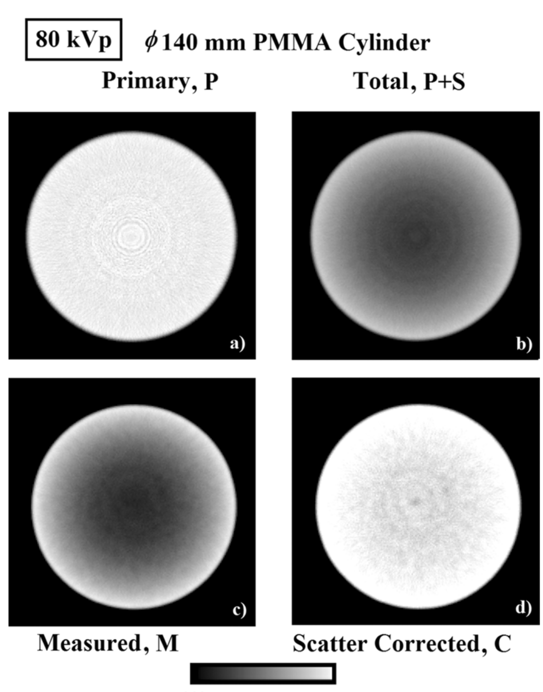

Fig. 8. Simulated primary (a), simulated total (b), measured (c) and scatter-corrected (d) reconstructed axial slices (at 80 kVp) of the 140-mm PMMA cylindrical phantom.

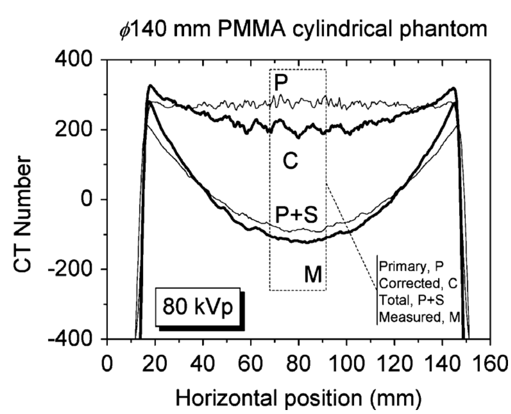

Fig. 9. Line profiles along the diameter of a 140-mm diameter PMMA cylinder on a reconstructed axial slice, at 80 kVp, obtained from simulated primary components only, from simulated total signal (primary plus scatter), from measurements and from measured data corrected for scatter.

TABLE II
CUPPING INDEX t_{cup}, NOISE AND FIGURE OF MERIT Q CALCULATED INSIDE A "MEASURED" (M) AND IN A "SCATTER-CORRECTED" (C) AXIAL SLICE, WHERE THE PHANTOM DIAMETER IS 140 MM (CYLINDER) OR 118 MM (HEMI-ELLIPSOID)

Phantom ϕ140 mm	t_{cup}		Noise		Q
	Uncorrected (M)	Corrected (C)	Uncorrected (M)	Corrected (C)	
Cylinder	25%	6%	3%	3%	0.98
Ellipsoid	23%	7%	3%	2%	0.96

breast tissue were obtained; the corresponding horizontal and vertical profiles are shown in Fig. 13. These plots show that the lower-density breast phantom (0.959 g/cm^3 vs. 1.19 g/cm^3 for PMMA) generates some greater scatter at the center of the phantom but with a much reduced SPR (about 0.5 for breast and 0.7 for PMMA, at maximum), with respect to the PMMA phantom. These data show that PMMA as a phantom material

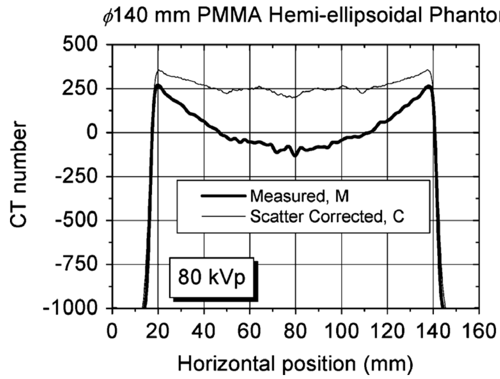

Fig. 10. Line profiles along the diameter of a 140-mm diameter PMMA hemi-ellipsoidal phantom on a reconstructed axial slice obtained from measurements at 80 kVp (thin line) and from measured data corrected for scatter via subtraction of simulated axial slice (thick line).

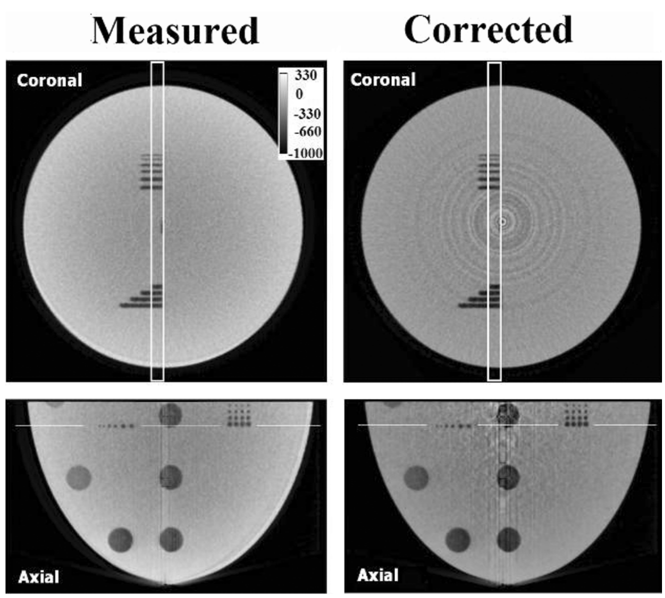

Fig. 11. Reconstructed mid-plane axial (bottom row) and coronal (upper row) CT slices (at 80 kVp) of 140-mm diameter PMMA phantom from acquired dataset (left column) and from a corresponding scatter-corrected dataset (right column). Internal air-filled holes are visible. A rectangular ROI is indicated on the coronal slice for evaluation of the average line profile. The horizontal dashed white line in the axial slices indicates the axial level at which the coronal slices have been selected.

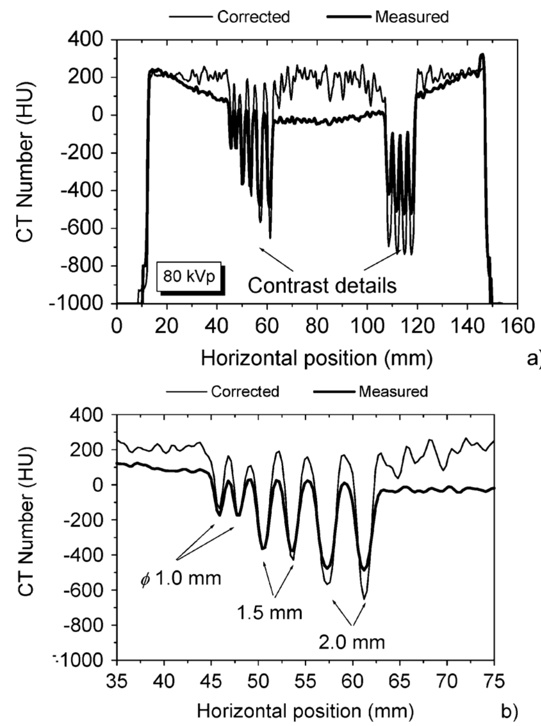

Fig. 12. (a) Average line profile in the rectangular ROI shown in Fig. 11, for both measured and scatter corrected CT slices. (b) Magnified view of one set of details (hole diameter 1, 1.5, 2 mm) in the line profiles shown in (a), indicating that no loss in spatial resolution is accompanied with the proposed correction procedure.

can roughly approximate the attenuation and scatter of a breast tissue having a VGF close to 13%.

IV. Discussion

A. Scatter Correction

The method described in this paper enables scatter correction via subtraction of the simulated scatter component from projections before reconstruction, without increasing the X-ray dose delivered to the patient, thus avoiding a major disadvantage of correction schemes involving anti-scatter grids [23], [45] or on-line beam-stops scatter measurement [25]. This method consists of an MC estimation of the scattered radiation image within the breast, assuming a breast shape and average composition. Data in Table II give an evaluation of the proposed scatter correction procedure: for a PMMA phantom of $\phi 140$ mm there is a reduction of the cupping artifact by a factor 4 (from 25% to 6%) for the cylindrical shape, and by a factor 3 (from 23% to 7%) for the hemi-ellipsoidal shape, for phantoms of almost the same volume. The residual cupping could be in part attributed to energy dependence of the detector response, which was not simulated in this study. Moreover, after scatter correction no increase of image noise is observed (Table II).

The quality of scatter correction can be analyzed in terms of the figure of merit Q introduced in [43] with reference to a scatter correction algorithm in flat-detector CT for head, hip and thorax phantoms; in that paper, a Q value of 0.82, 0.76 and 0.77 was reached, respectively ($Q = 1$ for the case of ideal correction). In the present work, for a PMMA breast phantom of 140-mm diameter, a Q value of 0.98 and 0.96 was reached for a cylindrical and for a hemi-ellipsoidal shape, respectively. This indicates that though a significant correction of the cupping artifact due to scattering is reached with the proposed method, there is still a residual cupping which is not explained in the present simulations. This source of cupping seems not to be due to the beam hardening, which is almost absent in the axial profile reconstructed from the primary beam (Fig. 9(a)). The unexplained source of cupping could be attributed to underestimation of the total scattering in the MC simulations with respect to measurements. Indeed, in Fig. 6(a) (140-mm cylinder), the relative difference $(\mathrm{P+S-M})/(\mathrm{P+S})$ is $-(2{\pm}2)\%$ $(\mathrm{mean} \pm \mathrm{std.\ dev.})$

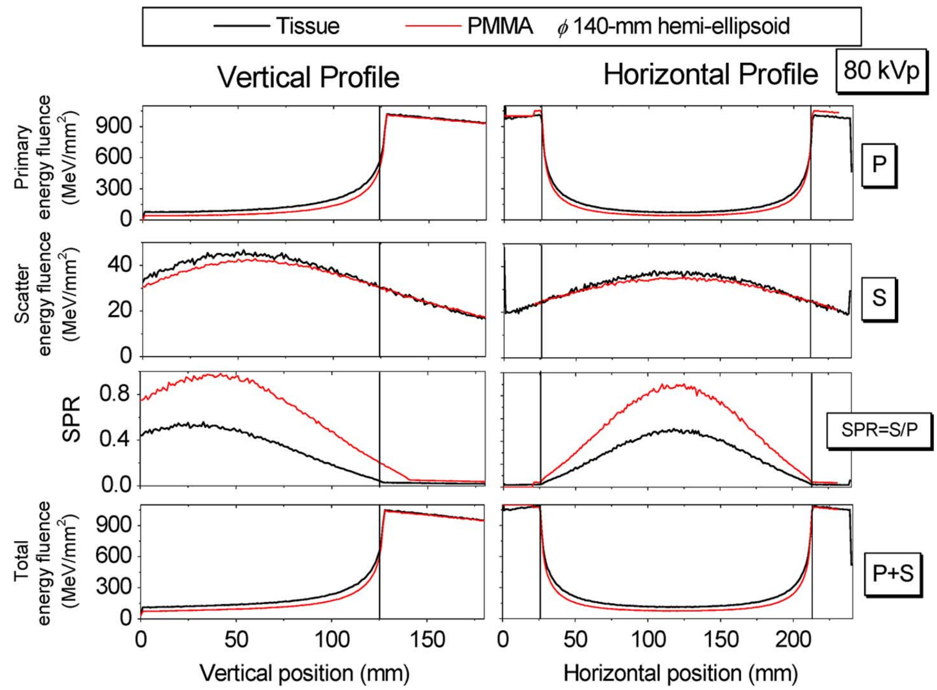

Fig. 13. Vertical and horizontal profiles along the primary (P), scatter (S), total $(\mathrm{P}+\mathrm{S})$ and SPR images for the hemi-ellipsoidal phantoms of 140-mm diameter made either of PMMA ($\mathrm{density} = 1.19$ g/cm^3) (red or lighter line) or of breast tissue with 13% glandular and 87% adipose tissue fraction ($\mathrm{density} = 0.959$ g/cm^3) (black line), at 80 kVp. The vertical profiles were evaluated along the vertical central axis as the average profiles of 20 image columns. The horizontal profiles were determined at 100 mm from the top base as the average profile of 20 image rows. The vertical lines in the plots indicate the extension of the phantom.

in the 120-mm wide central part of the phantom. This deviation is large enough to explain the observed amount of residual cupping (6% and 7%, Table II) after the application of our correction procedure. On the other hand, noise does affect also uncertainty on the estimation of cupping, and noise is dose-dependent.

We note that while the detail contrast improves after the correction and the noise increases, in a contrast details analysis the CNR remained little affected by the correction procedure (values from 17 to 15) and, at the same time, the spatial resolution appeared practically unaffected, at least for the lowest size of the high contrast detail of 1 mm.

The results shown above point toward a sensitivity of the scatter removal procedure on the shape of the object. For example, from our findings one may infer the improvement in correcting the scan data for a realistic breast phantom (i.e., a hemi-ellipsoidal shape) rather than for a simple cylindrical geometry, since SPR patterns and scatter amounts are different in the two cases (Fig. 7).

Fig. 13 shows that for a PMMA hemi-ellipsoidal phantom of 140-mm diameter the total (i.e., $\mathrm{primary} + \mathrm{scatter}$), scatter and SPR distributions are approximately close to the corresponding distributions for a breast tissue phantom with a VGF of 13%. While in mammography there is a well-known correspondence in terms of X-ray attenuation between PMMA and breast tissue which is at the basis of glandular dose estimation, in CBBCT this correspondence is still to be investigated, since the beam qualities are completely different from mammography and the breast is uncompressed. Then, Fig. 13 suggests that in terms of X-ray scatter and total attenuation, at 80 kVp (and $\mathrm{HVL} = 5.6$ mm Al), PMMA can at least roughly approximate the uncompressed breast with a size of 140 mm at chest wall and tissue composition of 13% glandular and 87% adipose (volume fractions). PMMA is a very convenient material for tissue phantoms in CBBCT and when using PMMA breast phantoms, it would be useful to know the equivalence to breast tissue at the given beam quality. MC simulations, to be reported in a future work, will investigate systematically this correspondence with hemi-ellipsoidal phantoms of varying diameter, by analyzing total attenuation and scatter patterns and determining the VGF that gives rise to the same patterns as in a PMMA phantom of equal diameter.

The choice of a breast shape and composition for scatter estimation relies on parameters estimation from the measured CT slices. The concept of performing a preliminary tomographic reconstruction to correct scattered radiation in CBCT has already been investigated by Zbijewski *et al.* [28] who suggested to perform a first reconstruction to estimate scattered radiation on tomographic projections, using an MC code. The main drawback of techniques that use an MC code is the high computing time needed to obtain simulations that are sufficiently representative of actual situations [26]–[28]. On the other hand, in the method proposed here the MC simulations are performed prior to the CT scan and their results are available at the time of the CT scans, so that the reconstruction process is not slowed down. In mammography, some geometrical parameters, such as the thickness of the compressed breast, are known during examination, whereas in CBBCT, the geometrical shape of the breast is unknown until the reconstruction and a dedicated software data analysis phase, e.g., as shown in [44]. Without prior geometrical parameters, it remains difficult to precisely estimate scattered radiation in an analytical manner. Thus, in CBBCT one could first impose a known shape to the breast (e.g., with a breast-holder) and then assume the scattered-radiation pattern for a given composition of the breast tissue (e.g., according the VGF parameterization provided in [44]). Moreover, the use of a breast holder placed at the scanner isocenter allows to eliminate the need for a scout scan of the breast, as suggested for example in [25] where this preliminary scan for centering the breast in the FOV is used for scatter estimation as well with the BSA method. In this way, there would be no extra dose to the patient in practice.

B. Use of a Breast Holder

In the following we will discuss in some detail the idea we derived from the present investigation, of a method for scatter correction based on MC simulations and on the use of a breast holder during acquisition (e.g., in the form of a hollow shaped PMMA cup of given length-to-diameter ratio for given bra size), in order to obligate the breast in a known form and in a given position in the FOV.

The shape of the breast holder could be selected in terms of the descriptors outlined in a recent work [44] based on the bra cup size (see below); alternatively, as a preliminary choice, in this work a hemi-ellipsoidal breast shape was analyzed (as done, e.g., in [8], [12], [50], [13], [22], with a PMMA breast phantom). The use of a pre-shaped holder giving to the breast a rough pre-known shape would permit the creation of a scatter distribution database for a given holder size, obtained by MC imaging simulation for a breast tissue volume of given glandularity and given holder geometry (e.g., classified in terms of bra cup sizes), at a known magnification. No extra dose to the patient is required for the creation of this database. Then, the signal component due to the primary photons in the projections would be estimated by subtracting the simulated scatter patterns from the raw acquired projections.

The assumption of a breast model based on few descriptors derives from the analysis of a recent work by Huang *et al.* [44]. They provided measurements of breast diameter, length, shape, volume glandular fraction and fibroglandular tissue distribution in 210 women. They found that bra cup size “may be a rough classification of breast size with respect to these metrics”. Specifically, the mean breast diameters at chest wall (± standard error) for bra cup sizes A, B, C, and D were $111\pm5, 114\pm3, 130\pm2$, and 137 ± 2 mm, respectively, and corresponding mean breast lengths (from chest wall toward the nipple) were $57\pm5, 71\pm3, 94\pm2$, and 97 ± 2 mm, respectively. In considering the distribution of percent glandular tissue volume over glandular plus adipose tissue (VGF), it ranged from about 24% (for 80-mm breast diameter) to 8% (for 160-mm breast diameter); no significant correlation of VGF with the cup size was shown. Overall, all these findings [44] can be considered as the basis for a parametric description of the average uncompressed, pendant breast shape and size in terms of a few descriptors (bra cup size, breast profile shape, breast length, average VGF) in order to determine a set of “average breast phantoms” useful for scatter estimation and correction in CBBCT. On this basis, a set of suitable breast holders could be realized (e.g., see Fig. 1(c)).

The use of a breast holder would also have the effect of reducing the organ motion. This would reduce also the motion artifact of the freely pending breast, during a long scan time. In addition to patient comfort, the use of longer scan times permits the use of lower x-ray tube currents as available with microfocus x-ray tubes: use of such a highly coherent source would improve the visibility of phase-contrast effects (e.g., edge-enhancement of lesion borders or improved visibility of microcalcifications) in phase-contrast imaging conditions [13], [46]. Such an experimental task is underway in our laboratory, after first observations of phase-contrast effects in CBBCT scans of a test object [47].

For scatter correction in clinical conditions, a set of four scatter distributions for the four classes of breast size (and corresponding breast glandularity) can then be determined via MC simulations. This set is calculated for given scan parameters (kVp, imaging geometry): through the use of the breast holder placed at the isocenter, the scan geometry is pre-determined for all breast scans.

Exploiting the axial symmetry of the breast geometry in the holder, each distribution will contain full-field scatter projections from just a limited set of views (e.g., 36 views over 360 deg), calculated with a photon statistics comparable to the corresponding acquired projections. This would require, e.g., in the order of 10^9 photon histories in the MC simulation for calculating the scatter distribution in each view. Assuming, for example, 36 views, this would require 375 h CPU time per dataset in the same condition of this study (where launching a total of 1.44×10^9 histories per scan required 15 h CPU time). Variance reduction techniques are available, however (e.g., [35], [48]), to reduce the huge computation time of MC based scatter correction strategies to $\sim$1 h or less.

The PMMA breast phantom used in this study has a CT number $\sim$250 HU at 80 kVp; it has been calculated [49] that adipose and fibroglandular breast tissues have a CT number of -240 and 35 HU, respectively, at 80 kVp, so showing a contrast of 275 HU; for comparison, we note that in [49] a gelatin breast phantom with CT number $\sim$185 HU was adopted, as mimicking the fibroglandular tissue component. Our PMMA phantom showed a higher CT number (at 80 kVp), more similar to glandular than to adipose tissue.

In the present study, measurements (and corresponding simulations) were done with an object-to-detector distance of just 120 mm, at a magnification of 1.31, with a corresponding air gap of just a few cm between the phantom and the detector. This reduced air gap is known to determine a high scatter and corresponding high SPR in the projections [20], [22]. By increasing the object-to-detector distance from 120 mm to, e.g., 270 mm ($\text{magnification} = 1.7$, still manageable in our setup), a 140-mm breast size (diameter at the chest wall, corresponding to cup size D) would still be imaged in the FOV of a 240 × 240 mm^2 detector, but the air gap would be increased to 200 mm. In such conditions, from results of MC simulations in our previous work [22] we anticipate a reduction of the scatter intensity by a factor as large as $\cong 4$ with respect to a 120-mm air gap. This would be another by-result of the breast-holder technique, since even large breasts could be compressed in the holder to a D-class size and imaged at a magnification yielding a large air gap, with a 240×240 mm^2 or larger detector.

V. Conclusion

A scatter correction technique was developed in which the MC predicted scatter distribution is scaled in intensity and then subtracted from the projections prior to reconstruction. Laboratory tests of the procedure were done with homogeneous PMMA phantoms with a cylindrical or a hemi-ellipsoidal shape. Profile measurements were obtained for scatter-corrected and uncorrected images. The technique has shown to be effective in largely removing the cupping artifact due to scatter, thus improving the CT image uniformity. A method, based on the use of a breast holder and a MC scatter-correction algorithm, has been discussed for a flat panel detector-based cone-beam breast CT scanner. Scatter patterns could be generated in advance of scanning, on the basis of a parametric representation of the breast size and composition suggested by recent literature data. The heavy computing task for such a MC simulation would be limited to just four datasets for the corresponding classes of bra cup size, for given technique factors and scan geometry.

References

[1] R. H. Johnson *et al.*, "Feldkamp and circle-and-line cone-beam reconstruction for 3D micro-CT of vascular networks," *Phys. Med. Biol.*, vol. 43, pp. 929–940, 1998.

[2] M. A. Mosleh-Shirazi, P. M. Evans, W. Swindell, S. Webb, and M. Partridge, "A cone-beam megavoltage CT scanner for treatment verification in conformal radiotherapy," *Radiother. Oncol.*, vol. 48, pp. 319–328, 1998.

[3] D. A. Jaffray and J. H. Siewerdsen, "Cone-beam computed tomography with a flat-panel imager: Initial performance characterization," *Med. Phys.*, vol. 27, pp. 1311–1323, 2000.

[4] D. Letourneau *et al.*, "Cone-beam-CT guided radiation therapy: Technical implementation," *Radioth. Oncol.*, vol. 75, pp. 279–286, 2005.

[5] K. Maki, N. Inou, A. Akanishi, and A. J. Miller, "Computer-assisted simulations in orthodontic diagnosis and the application of a new cone beam x-ray computed tomography," *Orthod. Craniofac. Res.*, vol. 6, pp. 95–101, 2003, Suppl. 1.

[6] I. Hein, K. Taguchi, M. D. Silver, M. Kazama, and I. Mori, "Feldkamp based cone-beam reconstruction for gantry-tilted helical multislice CT," *Med. Phys.*, vol. 30, pp. 3233–3242, 2003.

[7] J. M. Boone, T. R. Nelson, K. K. Lindfors, and J. A. Seibert, "Dedicated breast CT: Radiation dose and image quality evaluation," *Radiology*, vol. 221, pp. 657–667, 2001.

[8] B. Chen and R. Ning, "Cone-beam volume CT breast imaging: Feasibility study," *Med. Phys.*, vol. 29, pp. 755–770, 2002.

[9] S. J. Glick, "Breast CT," *Annu. Rev. Biomed. Eng.*, vol. 9, pp. 501–526, 2007.

[10] M. P. Tornai *et al.*, "Design and development of a fully 3D dedicated x-ray computer mammotomography system," in *Proc. SPIE*, 2005, vol. 5745, pp. 189–197.

[11] W. T. Yang *et al.*, "Dedicated cone-beam breast CT: Feasibility study with surgical mastectomy specimen," *Amer. J. Roentgenol.*, vol. 189, pp. 1312–1315, 2007.

[12] P. Russo, A. Lauria, G. Mettivier, and M. C. Montesi, "X-ray cone-beam breast computed tomography: Phantom studies," in *Proc. IEEE Nucl. Sci. Symp. Conf. Rec.*, 2008, pp. 4803–4810.

[13] G. Mettivier *et al.*, "Dedicated scanner for laboratory investigations on cone-beam CT/SPECT imaging of the breast," *Nucl. Instrum. Meth. A*, vol. 629, pp. 350–356, 2011.

[14] A. M. O'Connell, D. L. Conover, and C. L. Lin, "Cone-beam computed tomography for breast imaging," *J. Radiol. Nurs.*, vol. 28, pp. 3–11, 2009.

[15] K. K. Lindfors *et al.*, "Dedicated breast CT: Initial clinical experience," *Radiology*, vol. 246, pp. 725–733, 2008.

[16] N. D. Prionas *et al.*, "Contrast-enhanced dedicated breast CT: Initial clinical experience," *Radiology*, vol. 256, pp. 714–723, 2010.

[17] E. P. Ruhrnschopf and K. Klingenbeck, "A general framework and review of scatter correction methods in x-ray cone-beam computerized tomography. Part 1: Scatter compensation approaches," *Med. Phys.*, vol. 38, pp. 4296–4303, 2011.

[18] E. P. Ruhrnschopf and K. Klingenbeck, "A general framework and review of scatter correction methods in x-ray cone-beam computerized tomography. Part 2: Scatter estimation approaches," *Med. Phys.*, vol. 38, pp. 5186–5199, 2011.

[19] J. H. Siewerdsen and D. A. Jaffray, "Cone-beam computed tomography with a flat panel imager: Magnitude and effects of x-ray scatter," *Med. Phys.*, vol. 28, pp. 220–231, 2001.

[20] A. L. C. Kwan, J. M. Boone, and N. Shah, "Evaluation of x-ray scatter properties in a dedicated cone-beam breast CT scanner," *Med. Phys.*, vol. 32, pp. 2967–2975, 2005.

[21] Y. Chen *et al.*, "Characterization of scatter in cone-beam CT breast imaging: Comparison of experimental measurements and Monte Carlo simulation," *Med. Phys.*, vol. 36, pp. 857–869, 2009.

[22] G. Mettivier, P. Russo, N. Lanconelli, and S. L. Meo, "Evaluation of scattering in cone-beam breast computed tomography: A Monte Carlo and experimental phantom study," *IEEE Trans. Nucl. Sci.*, vol. 57, pp. 2510–2517, 2010.

[23] M. Endo, T. Tsunoo, N. Nakamori, and K. Yoshida, "Effect of scattered radiation on image noise in cone beam CT," *Med. Phys.*, vol. 28, pp. 469–474, 2001.

[24] J. H. Siewerdsen *et al.*, "A simple, direct method for x-ray scatter estimation and correction in digital radiography and cone-beam CT," *Med. Phys.*, vol. 33, pp. 187–197, 2006.

[25] W. Cai, R. Ning, and D. Conover, "Simplified method of scatter correction using a beam-stop-array algorithm for cone-beam computed tomography breast imaging," *Opt. Engin.*, vol. 47, no. 097003, 2008.

[26] D. A. Jaffray, J. J. Battista, A. Fenster, and P. Munro, "X-ray scatter in megavoltage transmission radiography-physical characteristics and influence on image quality," *Med. Phys.*, vol. 21, pp. 45–60, 1994.

[27] G. Jarry *et al.*, "Monte Carlo investigation of scatter contribution to kilovoltage cone-beam computed tomography images," *Med. Phys.*, vol. 32, p. 2092, 2005.

[28] W. Zbijewski, A. P. Colijn, and F. J. Beekman, "Monte Carlo based scatter correction for cone-beam micro-CT," presented at the 7th Int. Conf. on Fully 3D Reconstruction in Radiology and Nuclear Medicine, Saint Malo, France, 2003.

[29] J. M. Boone and J. A. Seibert, "Monte-Carlo simulation of the scattered radiation distribution in diagnostic-radiology," *Med. Phys.*, vol. 15, pp. 713–20, 1988.

[30] G. Jarry *et al.*, "Characterization of scattered radiation in kV CBCT images using Monte Carlo simulations," *Med. Phys.*, vol. 33, pp. 4320–4329, 2006.

[31] A. P. Colijn and F. J. Beekman, "Accelerated simulation of cone beam x-ray CT scatter projections," *IEEE Trans. Med. Imaging*, vol. 23, pp. 584–590, 2004.

[32] W. Zbijewski and F. J. Beekman, "Efficient Monte Carlo based scatter artecat reduction in cone-beam Micro-CT," *IEEE Trans. Med. Imaging*, vol. 25, pp. 817–827, 2006.

[33] Y. Kyriakou, T. Riedel, and W. A. Kalender, "Combining deterministic and Monte Carlo calculations for fast estimation of scatter intensities in CT," *Phys. Med. Biol.*, vol. 51, pp. 4567–4586, 2006.

[34] A. Malusek, M. Sandborg, and G. A. Carlsson, "CTmod—A toolkit for Monte Carlo simulation of projections including scatter in computed tomography," *Comput. Methods Programs Biomed.*, vol. 90, pp. 167–178, 2008.

[35] E. Mainegra-Hing and I. Kawrakow, "Fast Monte Carlo calculation of scatter corrections for CBCT images," in *J. Phys. Conf. Ser.*, 2008, vol. 103, pp. 12–17.

[36] G. Poludniowski, P. M. Evans, V. N. Hansen, and S. Webb, "An efficient Monte Carlo-based algorithm for scatter correction in keV cone-beam CT," *Phys. Med. Biol.*, vol. 54, pp. 3847–3864, 2009.

[37] L. Feldkamp, L. C. Davis, and J. W. Kress, "Practical cone-beam algorithm," *J. Opt. Soc. Am. A*, vol. 6, pp. 612–619, 1984.

[38] S. Agostinelli *et al.*, "GEANT4 a simulation toolkit," *Nucl. Instrum. Meth. A*, vol. 506, pp. 250–303, 2003.

[39] J. Allison *et al.*, "Geant4 developments and applications," *IEEE Trans. Nucl. Sci.*, vol. 53, pp. 270–278, 2006.

[40] K. Amako *et al.*, "Comparison of Geant4 electromagnetic physics models against the NIST reference data," *IEEE Trans. Nucl. Sci.*, vol. 52, pp. 910–918, 2005.

[41] J. M. Boone and J. A. Seibert, "An accurate method for computer-generating tungsten anode x-ray spectra from 30 to 140 kV," *Med. Phys.*, vol. 24, pp. 1661–1670, 1997.

[42] International Commission on Radiation Units and Measurements, "Tissue Substitutes in Radiation Dosimetry and Measurement," ICRU, Bethesda, MD, ICRU Report 44, 1989.

[43] M. Meyer, W. A. Kalender, and Y. Kyriakou, "A fast and pragmatic approach for scatter correction in flat-detector CT using elliptic modeling and iterative optimization," *Phys. Med. Biol.*, vol. 55, pp. 99–120, 2010.

[44] S.-Y. Huang *et al.*, "The characterization of breast anatomical metrics using dedicated breast CT," *Med. Phys.*, vol. 38, pp. 2180–2191, 2011.

[45] J. H. Siewerdsen, D. J. Moseley, B. Bakhtiar, S. Richard, and D. A. Jaffray, "The influence of antiscatter grids on soft-tissue detectability in cone-beam computed tomography with flat-panel detectors," *Med. Phys.*, vol. 31, pp. 3506–3520, 2004.

[46] W. Cai and R. Ning, "Preliminary study of a phase-contrast cone-beam computed tomography system: The edge-enhancement effect in the tomographic reconstruction of in-line holographic images," *Opt. Eng.*, vol. 47, no. 037004, 2008.

[47] G. Mettivier, M. C. Montesi, A. Lauria, and P. Russo, "Measurement of the MTF of a cone-beam breast computed tomography laboratory scanner," in *Proc. Nuclear Science Symp. Conf. Record (NSS/MIC)*, 2009, pp. 3958–3964.

[48] E. Mainegra-Hing and I. Kawracow, "Variance reduction techniques for fast Monte Carlo CBCT scatter correction calculations," *Phys. Med. Biol.*, vol. 55, pp. 4495–4507, 2010.

[49] J. C.-J. Lai *et al.*, "Visibility of microcalcification in cone beam breast CT: Effects of x-ray tube voltage and radiation dose," *Med. Phys.*, vol. 34, pp. 2995–3004, 2007.

[50] P. Russo, A. Lauria, G. Mettivier, and M. C. Montesi, "X-ray cone-beam breast computed tomography: Phantom studies," *IEEE Trans. Nucl. Sci.*, vol. 57, pp. 160–172, 2010.